Auto-Segmentation and Quantification of Non-cavitated Enamel Caries Imaged with Swept Source OCT

Tamer Abdelrehim * , Maha Salah , Alex Fok , Heather J Conrad , Hooi Pin Chew *

Posted Date: 30 October 2023

doi: 10.20944/preprints202310.1869.v1

Keywords: OCT; Micro CT; SEM; Image Segmentation; Carious; batch-processing; Simulation; Dental imaging; demineralization; Quantification

Article

Auto-Segmentation and Quantification of Non-cavitated Enamel Caries Imaged with Swept Source OCT

Tamer Abdelrehim[1,*], Maha Salah [1], Alex Fok[1], Heather Conrad[2] and Hooi Pin Chew[1]

[1] Minnesota Dental Research Center for Biomaterial and Biomechanics, University of Minnesota, 16-256B Moos Tower 515 Delaware St. SE, Minneapolis, Minnesota 55455, USA; tamerniskriss@gmail.com (T.A.); chew0014@umn.edu (H.C.)
[2] Department of Restorative Dentistry, University of Minnesota, 16-256B Moos Tower 515 Delaware St. SE, Minneapolis, Minnesota 55455, USA
* Correspondence: tamerniskriss@gmail.com (T.A.), chew0014@umn.edu (H.C.)

Abstract: (1) Background: OCT imaging has been used to assess enamel demineralization in dental research but is not yet developed enough to qualify as a diagnostic technique in clinics**. The current capabilities of most commercial acquisition software allow for visual and qualitative assessment. There is a need for a fast and verified batch-processing algorithm for segmenting and analyzing the demineralized enamel. This study suggests a GUI MATLAB algorithm for processing and quantitative analysis of the demineralized enamel.** (2) Methods: A group of artificially demineralized human enamels was in vitro scanned under the OCT, and ROI frames were extracted. By using a selected intensity threshold colormap, inter- (*Ie*) and intra- (*Ia*) prismatic demineralization can be segmented. A set of quantitative measurements for average demineralized depth, average line profile, and integrated reflectivity can be obtained for an accurate assessment. Real and **simulated OCT frames were used for algorithm verification.** (3) Results: A strong correlation between automated and known Excel measurements for the average demineralization depth was found ($R^2 > 0.97$). (4) Conclusions: OCT image segmentation and quantification of the enamel demoralization zones are possible. The algorithm can assess the future development of a real-time assessment of dental diagnostics using an oral probe OCT.

Keywords: OCT**;** Micro CT**;** SEM**;** Image Segmentation**;** Carious**;** batch-processing**;** Simulation; Dental imaging**;** demineralization; Quantification

1. Introduction

In dental caries research, there is a crucial need to be able to study demineralization, with high-resolution tomographic imaging technique that can be used both in vitro and in vivo especially intraorally. One of the important aspects of enamel demineralization studies is the design of preventive and remineralization materials, which requires an understanding of the temporal and spatial development of distinct ultrastructural early demineralized enamel zones as well as the diffusion-reaction mechanisms of the de- and remineralization processes [1-6]. Early demineralized enamel has two layers, according to previous studies: Intra- and interprismatic demineralization is the first layer to be observed after the enamel surface; interprismatic demineralization is the second layer beyond that; and healthy or sound enamel (*sound*) sits beyond this demineralization progression [7-10]. Transmission electron microscope (TEM) and scanning electron microscope (SEM) are key imaging tools used to visualize and study these demineralization zones. However, challenging aspects of using these microscopy techniques such as their destructive nature and the intricate sample preparation processes limits the use of these techniques to only a small number of sample size and makes monitoring temporal changes of the demineralization zones *in vitro* and *in vivo* impossible.

It has been noted that demineralized enamel or dentin possess altered optical characteristics compared to their *sound* status [11,12]. It is also noteworthy that at the beginning of the enamel caries process, the scattering coefficient of dental enamel increases considerably with increasing mineral loss. Substantial associations between mineral loss and near-infrared (NIR) scattering has been

 doi:10.20944/preprints202310.1869.v1

established [12,13] and optical coherence tomography (OCT) with the central wavelength of 1300 nm has been found to be particularly useful in assessing non-cavitated enamel demineralization because of its ability to provide non-invasive, depth-resolved, high-resolution near infra-red backscatter characteristics of demineralization. Moreover, the oral handheld OCT is considered extremely safer clinically than radiographs and gives more information in just one 3D scan. As a result, one area of OCT usage is the early diagnosis of enamel defects using the scattering coefficient. Research on the evaluation of demineralization of dental hard tissue using OCT started more than 20 years ago [12-22]. OCT's ability to detect minute cross-sectional optical and morphological changes of dental hard tissues without using ionizing radiation makes it advantageous, especially clinically.

Researchers have validated the qualitative distribution and pattern of OCT reflectance for fissure and smooth surface enamel caries against histological techniques such as polarized microscopy and confocal laser scanning microscopy and found good correlations [20,23,24] between them. Recently, a few studies had even reported using deep learning to classify these OCT reflectance distribution and patterns to detect caries [25,26].In addition to utilizing OCT reflectance pattern of enamel demineralization qualitatively, many quantitative outcome measures had been derived from OCT depth-resolved reflectance profile, in an attempt to quantify the severity of demineralization in both degree and depth of demineralization. Lesion depth, integrated reflectivity, and attenuation coefficients are among the quantitative outcome measures often utilized [18-21,27,28]. The relative changes of these outcome measures for enamel and dentin before and after an intervention, be it de- or remineralization, can be used to assess the effect of that intervention [29,30]. However, variations in these quantitative results between different studies have been found and this has been attributed to the different OCT systems used, sample preparations methods and the arbitrary nature of some of the outcome measures [31]. Demineralization or lesion depth is a much-favored outcome measure in most tomographic methods, such as Micro Ct and confocal microscopy, as it impacts clinical treatment decision making. Consequentially the same outcome measure has been explored on OCT reflectance. However, as the intensity range of OCT images is relatively wide, choosing an intensity threshold for the end point of a lesion proves to be a challenge. Le et al. [32] measured lesion depth using edge-finding algorithms whilst Can et al [33] chose the intensity threshold for lesion depth as $1/e^2$ times that of the peak intensity. Other studies [34-36] determine the lesion severity by integrating the reflectance of the OCT line profiles from the tooth surface to a selected depth. Integrated reflectance, however, can be affected by surface specular reflectivity and in some cases, the speckle noise combined with OCT scans. Therefore, it has been suggested that there is a need for more standardized and robust OCT methodologies to diagnose and quantify early enamel caries lesions [31], which include improvements of the OCT scanning hardware and also optimization of the data extraction and image processing process.

Different image processing methods had been explored on dental-related OCT reflectance, including an averaged intensity difference detection algorithm for gingival sulcus [37], a depth intensity profile analysis for detection of microdamage after implant insertion [38], and an intensity-based layer segmentation algorithm for the detection of enamel abrasion and wear [34], to name a few. These algorithms could potentially be adapted for the analysis of demineralized enamel and dentine. It has also been suggested that deep learning algorithms may more precisely segment demineralized areas [39], however, the algorithm not yet distinguish between inter- (*Ie*) and intra- (*Ia*) prismatic demineralization and have the limitation of manual verification even using Micro CT as a reference.

For longitudinal de- and remineralization studies and studies with large sample size, robust and targeted image processing methods such as segmentation of demineralization zones are needed to minimize manual and fatigue error and subjectivity during data extraction. This entails the need for a validated and streamlined data processing algorithm specific for demineralized tooth structure. In order to validate data processing algorithms, modulation and simulation of OCT signals has previously been done using Lab VIEW and MATLAB scripts [40].

This work reports on a verified automated algorithm to segment and measure the depth of *Intra-* and *Inter- prismatic* demineralization zones in early demineralized enamel scanned by swept-source

 doi:10.20944/preprints202310.1869.v1

optical coherence tomography (SS-OCT) images. This segmentation algorithm is based upon intensity thresholding previously identified using SEM [41].

2. Materials and Methods

2.1. Sample preparation and Optical Coherence Tomography scanning protocol (OCT)

Eight human extracted upper premolars with visually caries-free buccal surface were collected and cleaned. The crown of each tooth was then painted with an acid-resistant varnish except for approximately a 3 x 3 mm^2 window of the buccal surface. Each specimen were then subjected to different number of daily cycles of de-and remineralization ranging from 14 - 21 days (n = 1).The modified Featherstone pH cycling model was used [42] whereby the daily pH cycling routine consisted of demineralization for 6h in 40 ml of acid buffer (37°C) containing 2.0mmol/l Ca, 2.0 mmol/1 PO_4, 0.075 mol/1 acetate at pH 4.3, and then rinsed with deionized water and remineralization for 18 h (37°C) in 20 ml solution containing 1.5 mmol/1 Ca, 0.9 mmol/1 PO_4, 0.15 mol/ 1KCl, and 20 mmol/1 cacodylate buffer at pH 7.0.

The swept-source optical coherence tomography, SANTEC IVS-2000 SS-OCT, with a central wavelength of 1300nm and the SANTEC Innervision software was used to acquire the 3D OCT scans in this study. The OCT scanning protocol is described as follows; the 3 x 3 mm^2 demineralized region-of-interest was centralized in a scan area of 5 x 5 mm^2. The vertical distance of the specimens from the imaging probe was standardized with the highest point of the surface curvature positioned approximately at the 0.5 mm level of the Innervision imaging window. The scanning beam was oriented perpendicular to the buccal surface and configured to scan an area of 5 mm x 5 mm in the x-y direction and a depth of 1.85mm in enamel (refractive index = 1.63). The x-y-z pixel count was 256 × 256 × 1000, resulting in the lateral and axial resolution of 19.5 and 4.4 μm respectively.

2.2. Selection of the segmentation colormap, regions-of-interest and surface determination

The data extraction algorithm and an associated graphic user interface (GUI) were written using the MATLAB (R2015a, MathWorks) programming language [43]. Figure 1 shows a schematic diagram of the scanning method and main steps of the segmentation algorithm. The image acquisition software "Santec Inner Vision" and the OCT system were used to control the scan and choose the regions of interest (ROI) in the B-scan frames saved in "CSV" format. The frames can be cropped to the selected ROI to study a specific demineralized area and reduce the processing time, especially for large data sets. Our bespoke algorithm depends on a specific, previously determined color map threshold intensity [41]. This colormap can recognize early dental decay and distinguish three different levels of dental caries tissues, which are inter- (*Ie*) and intra- (*Ia*) *prismatic* demineralization zones and *sound* (healthy tissue) zones. The key idea for identification of the selected colormap is based on finding a good correlation between OCT and SEM frames after manual finding of the similar frames between OCT and SEM by superimposing the OCT frame with an automatic image segmentation for the SEM frames. The color map that will be used in the demoralization segmentation process is only chosen based on the best correlation results between OCT and SEM frames. The algorithm superimposes the two frames of OCT and SEM; if the two superimposed pixels are recognized with the same segmented zones, the logical result of the correlation is “true”; otherwise, it is “false”, The percentage of successively correlated area is then calculated for both zones. The selection of the demineralization color map can differ from other OCT or SEM specifications that are used for the correlation.

For the determination of the enamel surface, the determination of the background (air in this case) was first conducted. The average reflectance value of the background was attained from a known area of air immediately above the surfaces of 35 B-scans obtained from the 8 specimens. It was found that the threshold of 5 dB exceeds the background reflectance range and is below the sudden increase of reflectance at the enamel surface. Thereafter, the script locates and designates the first pixel in each depth-resolved reflectance line profile (A-scan) that is higher than the mean reflectance value of air as the surface.

Preprints (www.preprints.org) | NOT PEER-REVIEWED | Posted: 30 October 2023 doi:10.20944/preprints202310.1869.v1

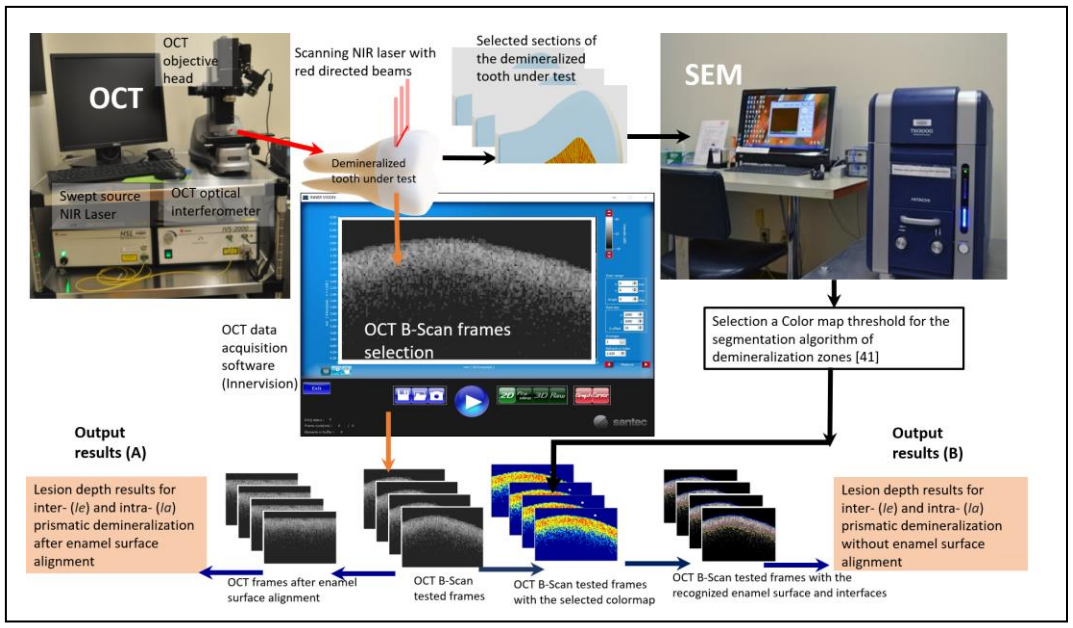

Figure 1. Schematic diagram of the scanning method and main steps of the segmentation algorithm.

2.3. Labelling of the inter- (Ie) and intraprismatic (Ia) demineralization zones

Upon determining the surface, the algorithm then labels air, sound enamel and the inter- and intra- prismatic demineralization zones with discrete colors based on the previously selected OCT intensity colormap defined in section (2.2) and used for the segmentation of these different zones. In this case, the segmentation algorithm labeled a color red for the intra- prismatic (*Ia*) demineralization zone, yellow for the interprismatic (*Ie*) demineralization zone, blue for sound enamel and dark blue for air (Figure 2a). The demineralization patterns of the 14 – 21 days caries lesions induced by the caries model used in this study [41] presented with distinct zones of inter- (*Ie*) and intra- prismatic demineralization (*Ia*) with the *Ia* zone located nearer to the surface and the *Ie* zone located deeper to the *Ia* zone. This means that the *Ia* zone is at the demineralization front of the caries lesion as shown in (Figure 2a).

2.4. Quantification of mean depths of the inter- (D_{Ie}) and intraprismatic (D_{Ia}) demineralization zones

Due to the curvature nature of enamel surface, the mean depths of inter- (D_{Ie}) and intra-prismatic (D_{Ia}) demineralization zones were computed both with the original surface curvature and with the enamel surface aligned flat.

2.4.1. Original curved surface

As shown in (Figure 2b), A combined image of the original OCT file is overlayed with the determined enamel surface (in blue) and the limits of the intra- prismatic *Ia* (in red) and inter-prismatic *Ie* (in yellow) zones. These limits are determined as the last axial pixel of every segmented zone at every A-line (From the surface to the bottom of the frame on the enamel tissue).

To measure D_{Ia} and D_{Ie} of curved enamel surface, firstly, the tangent angles of each pixel of the identified surface were determined using the "*skeletonOrientation*" MATLAB function (Figure 3a) and the median tangent angle, α was calculated. With the median tangent angle, it was then possible to determine the location of the deepest pixel of the *Ie* and *Ia* zones along the normal of each pixel on the surface.

The computation of the mean depths for the inter- (D_{Ie}) and intraprismatic (D_{Ia}) demineralization zones are described in Equations 1 and 2 below.

$$D_{Ia} = \frac{1}{n}\sum_{i=1}^{n}(\Delta Ia)_i * {Ps_{axial}}/{\cos\alpha} \quad (1)$$

Preprints (www.preprints.org) | NOT PEER-REVIEWED | Posted: 30 October 2023 doi:10.20944/preprints202310.1869.v1

$$D_{Ie} = \frac{1}{n}\sum_{i=1}^{n}(\Delta Ie)_i * {Ps_{axial}}/{\cos\alpha} \quad (2)$$

where, i is the pixel order along the enamel surface, n is the total number of pixels along the enamel surface, α is the median of the tangent angle along the enamel surface, Ps_{axial} is the axial pixel resolution, $(\Delta Ia)_i$ and $(\Delta Ie)_i$ are the axial depths at pixel (i) for the Ia and Ie zones respectively, measured from the enamel surface to the deepest pixel of each zone.

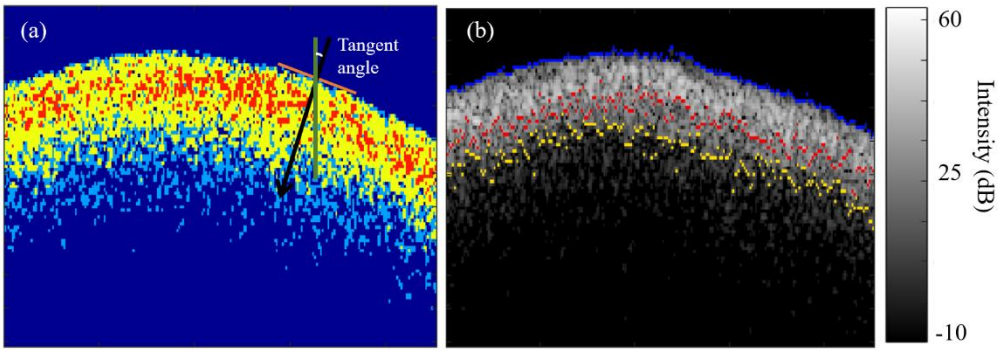

Figure 2. Quantification of mean depths of the inter- (D_{Ie}) and intra- prismatic (D_{Ia}) demineralization zones with the original surface curvature. a) The intra- prismatic (*Ia*) demineralization zone, interprismatic (*Ie*) demineralization zone, sound enamel and air were labelled red, yellow, blue and dark blue respectively. The red line is the tangent of one of the identified surface pixels. The tangent angle on is the angle between the normal of the enamel surface (black arrow) and the vertical axis (green line) b) A combined image of the original OCT file is overlayed with the determined enamel surface (in blue) and the limits of the *Ia* (in red) and *Ie* (in yellow) zones.

Figure 3 shows an example of an original B-scan before and after enamel surface alignment to an axial level corresponding to the highest axial point (dashed red line) on the original enamel surface.

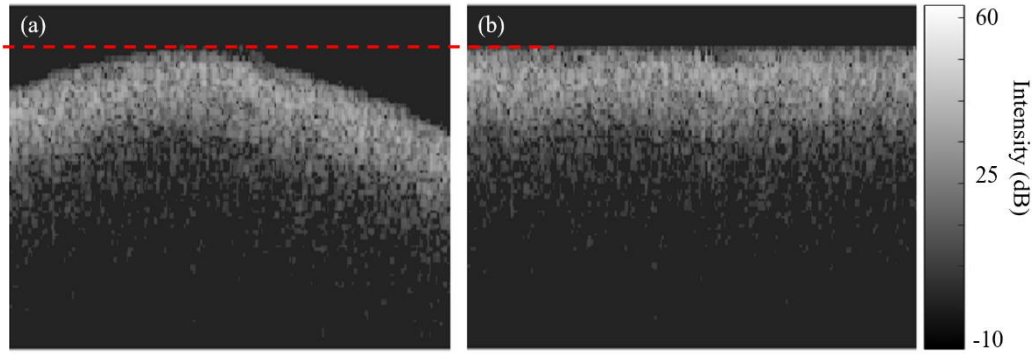

Figure 3. Enamel surface alignment. a) Original B-scan showing surface curvature and b) the same B-scan in (a) after enamel surface alignment to an axial level corresponding to the highest axial point (dashed red line) of the original enamel surface.

2.4.2. With aligned surface

The computation of the mean depths for the inter- (DlI_e) and intra- prismatic (DlI_a)demineralization zones after surface alignment are described in Equations 3 and 4 below.

$$DlI_a = \frac{1}{n}\sum_{i=1}^{n}(\Delta LIa)_i * Ps_{axial} \quad (3)$$

$$DlI_e = \frac{1}{n}\sum_{i=1}^{n}(\Delta LIe)_i * Ps_{axial} \quad (4)$$

Where, i is the pixel order along the enamel surface, n is the total lateral pixel number along the enamel surface, Ps_{axial} is the axial pixel resolution, $(\Delta LIa)_i$ and $(\Delta LIe)_i$ are the axial depths after

Preprints (www.preprints.org) | NOT PEER-REVIEWED | Posted: 30 October 2023 doi:10.20944/preprints202310.1869.v1

enamel surface alignment at pixel i for the Ia and Ie zones respectively and measured from the enamel surface to the deepest pixel of each zone.

2.5. Algorithm verification using simulated OCT B scans

To verify the output from the algorithm described above and to determine its limitations in segmenting the demineralization zones and measuring the demineralization depth, the verification was conducted in two phases. In phase I, twenty-three synthetic OCT B-scans were generated to simulate demineralized enamel of various stages. The key idea of using simulated OCT B-scans of demineralized enamel was to uncover errors in the algorithm using simulated B-scans with predefined line profiles (A-scans) of demineralized enamel and with known mean depths of the inter- (D_{Ie}) and intraprismatic (D_{Ia}) demineralization zones a priori.

The simulated B-scan required a predetermined A-scan and enamel surface profile. The simulated B-scan was generated by repeating the simulated A-scan laterally across the simulated enamel surface.

To simulate A-scans of demineralized enamel, three techniques were used:

1. Real average A-scan (RA_line), obtained from B-scans acquired from the specimens with known D_{Ie} and D_{Ia}
2. Least-square-fit A-scan (LS_line), obtained by fitting an A-scan of an acquired B-scan with a polynomial of degree 20. The MATLAB function *polyval* was used for curve fitting.
3. Mathematical A-scan (MA_line), obtained by using a combination of fundamental mathematical functions.

A typical A-scan of demineralized enamel consists of a sharp rise from the background value in signal intensity at the enamel surface due to specular reflection, followed by some high backscatter intensities from the demineralized lesion zone, and then an exponential decay with an attenuation coefficient for *sound* enamel. The OCT A-scan has been described by others using the Beer-Lambert law [44], i.e.

$$I(z) \propto exp^{-2\mu_t z} \tag{5}$$

where I is the reflected signal intensity, μ_t is the attenuation coefficient of enamel, z is the axial depth measured from the enamel surface, and the number "2" refers to the round-trip of light inside on the tissue and reflect to return and optically interfere with the OCT reference beam. The attenuation coefficient includes the absorption and scattering coefficient. Because the optical properties of teeth change after demineralization, the attenuation coefficients of *sound* and carious enamel differ [17,45]. The acquired A-scans of demineralized enamel are more complex than equation (5) indicates. In theory, there is a step change in signal intensity at the enamel surface. But because of its finite spatial resolution, the OCT scan has a more gradual increase in signal strength at the surface instead. The thin layer of demineralized enamel also produces a narrow plateau underneath the surface. The actual OCT A-scan can be modeled using a combination of two exponential decays with a more gradual initial rise, i.e.

$$I(z) = I1(z) + I2(z\ [z1{:}\ z2]) \tag{6}$$

$$I1(z) = az\ exp^{-2\mu_{t1} zS} + bz\ exp^{-2\mu_{t2} zS} \tag{7}$$

$$I2(z\ [z1{:}\ z2]) = I1(z\ [z1{:}\ z2]) * M \tag{8}$$

where a and b are constants, S is a scale parameter (in this simulation $S = 0.125$), M is a magnification parameter for the caries signal, and μ_{t1} and μ_{t2} are the attenuation coefficients for *sound* and demineralized enamel, respectively. The second function $I2$ describes the signal profile in the demineralization zone between $z1$ and $z2$. The scale parameter S is used to control the exponential damping of the simulated oct signal and then change the whole demineralization depth,

Preprints (www.preprints.org) | NOT PEER-REVIEWED | Posted: 30 October 2023 doi:10.20944/preprints202310.1869.v1

while the magnification parameter M is used to controls the reflection maximum intensity for interprismatic (*Ie*) demineralization zone.

To simulate the tooth surface, four different curvatures were used:

1. A flat tooth surface (F_sur).
2. The tooth surface from a real B-scan (S_sur).
3. A curved tooth surface generated using a cosine function (M_sur).
4. An irregular tooth surface drawn freehand by using MATLAB's freehand function (D_sur).

Figure 4 shows examples of some simulated OCT frames of demineralized enamel used for algorithm verification.

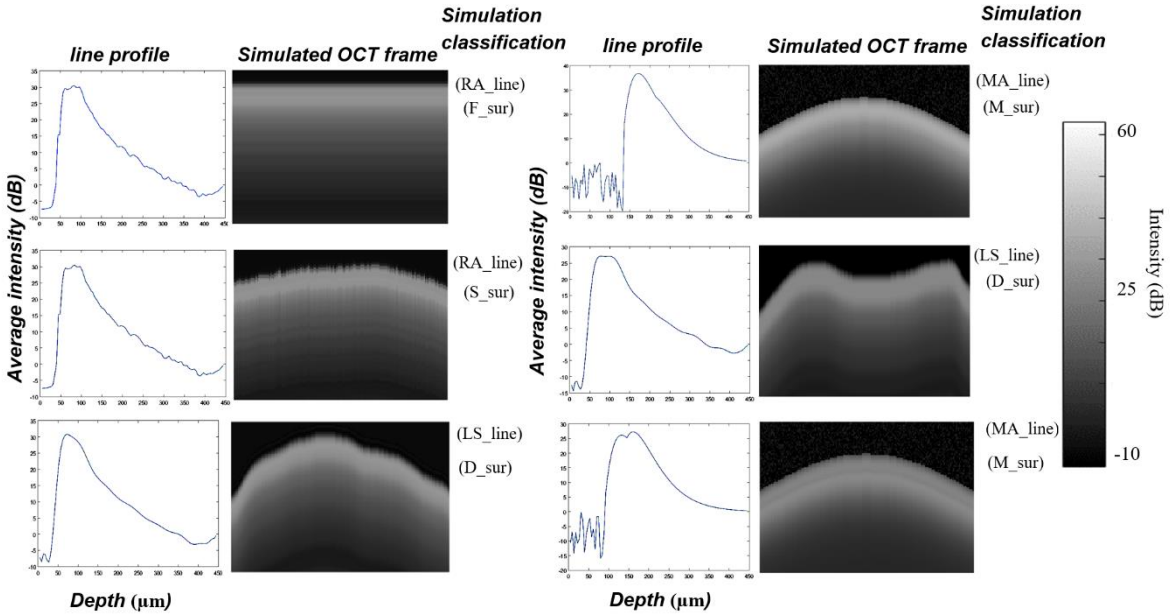

Figure 4. Example of different simulated OCT line profiles and B-scans of demineralized enamel for code validation. For A-scan simulation, (RA_line): Real average A-scan, (LS_line): Least square fitting A-scan, and (MA_line): Mathematical approach A-scan. For tooth surface curvature simulation, (F_sur): flat tooth surface, (S_sur): same surface as a selected real B-scan frame, (M_sur): mathematical equation surface, and (D_sur): freehand drawing surface.

In phase II of the verification process, twelve acquired B-scans from the 8 demineralized specimens were processed manually in a Microsoft Excel spreadsheet based on the same selected OCT intensity colormap and with the algorithm, and the extracted demineralization depth measurements were compared to determine the magnitude of deviations between the two measurements.

3. Results

The Phase I verification process did not reveal errors in the algorithm and the output D_{Ia} and D_{Ie} of the 23 simulated B-scans were as per the pre-determined measures.

As for the Phase II verification process, comparison of D_{Ia} and D_{Ie} of the 12 acquired B-scans were made between that computed manually and that by the algorithm both with and without surface alignment. The results of D_{Ia} and D_{Ie} from aligned and original curved surface were almost identical (Figure 5a and Figure 5c) and the R^2 value for the correlations between manually and algorithm computed D_{Ia} and D_{Ie} were 0.97 (Figure 5b and 5c) and 0.99 (Figure 5e and 5f) respectively. The mean difference between D_{Ia} and D_{Ie} computed with the algorithm and manually for the 12 acquired B-scans is 2.6 um with a standard deviation of 3.3 um, i.e., less than one pixel of axial resolution of 4.4 μm.

Preprints (www.preprints.org) | NOT PEER-REVIEWED | Posted: 30 October 2023 doi:10.20944/preprints202310.1869.v1

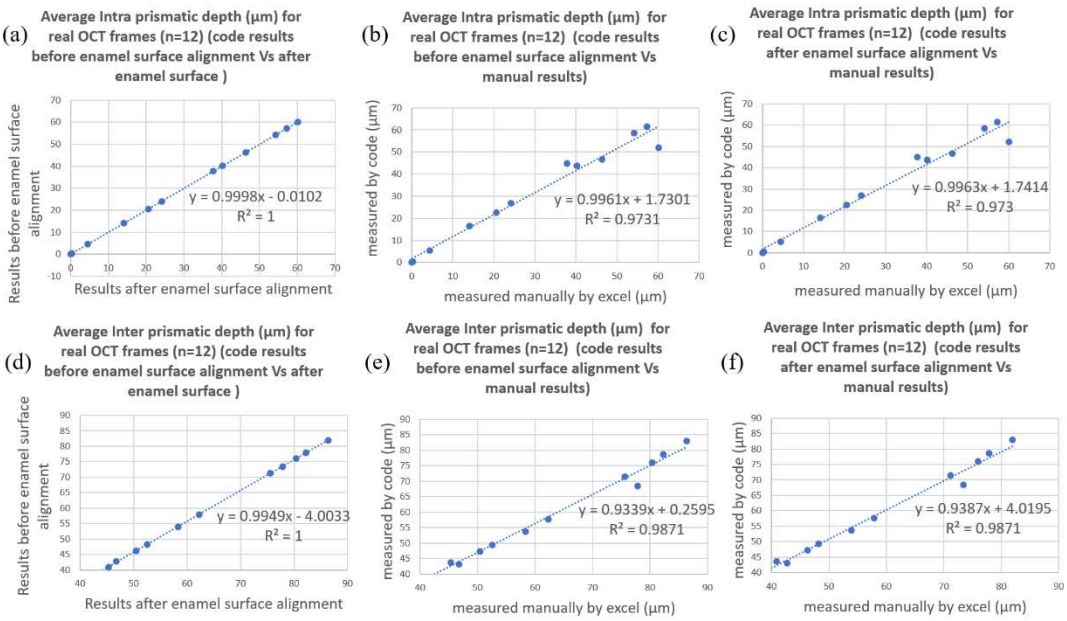

Figure 5. Correlation trendlines of the D_{Ia} and D_{Ie} of acquired OCT frames (n=12). The results of D_{Ia} and D_{Ie} from aligned and original curved surface were almost identical (Figure a and c) and the R^2 value for the correlations between manually and algorithm computed D_{Ia} and D_{Ie} were 0.97 (Fig b and c) and 0.99 (Figure e and f) respectively.

4. Discussion

Segmentation of biological structures in OCT scans is the most important image processing step to either qualitatively classify the biological structures or quantitatively measure their geometry. An automated segmentation process would be especially invaluable to facilitate clinicians making objective diagnoses and to extract large amounts of quantitative volumetric data in longitudinal clinical trials. There are many segmentation methods, such as thresholding, edge detection, and clustering [46]. Thresholding is by far the most common segmentation method used. The thresholding method labels pixels that have an intensity lower or higher than a pre-determined level, resulting in a binarized image, and this method can be subdivided into either global or local. The global thresholding method is based on finding a specific percentile of the image intensity histogram [47] and is widely used for surface determination. The local adaptive thresholding method, on the other hand, uses first-order statistics such as the mean, median, or standard deviation of the pixel intensity within each considered neighborhood to determine the threshold for each pixel and has been used to determine lesion depth. The edge detection method is based on uncovering intensity gradients along specific directions. It locates the edges where either the first derivative of intensity is greater than a particular threshold or the second derivative has zero crossings. After the edges have been detected, they form the object boundaries to segment the required regions and have been used in the determination of lesion depth in many studies [28, 48]. The Sobel and Canny operators are some of the most common edge detection algorithms. Another segmentation method that has not been used much is clustering [46]. Clustering is the grouping of similar instances, objects, or pixels [49]. The method of grouping pixels together could either be intensity-related [50] or structure-related or region-based using pre-annotated data [51]. It has been suggested that this clustering method is less susceptible to speckle noise and more useful for real problems or applied situations [52].

Our algorithm is a hybrid of global thresholding and multi-level quantized intensity threshold methods, where global thresholding was used for removing the background (air) and surface determination, and multi-level quantized intensity threshold was used to group the range of intensities to specific demineralization zones in enamel [41]. Speckle noise reduction with filters such as the median and gaussian filters was also not necessary as a pre-segmentation step. Following the establishment of the auto-segmentation technique, but prior to its use for the extraction of large

 doi:10.20944/preprints202310.1869.v1

amounts of data, systematic verification of the model or the full executable operations is critical to ensuring it does not demonstrate unintended behavior or harbor design errors. Verification is also necessary to assess its coverage, i.e., the extensiveness of its applicability. For this, verification was conducted in two phases. Two phases of the verification process were performed, i.e., against simulated and acquired A-scans of demineralized enamel, and we demonstrated that the results matched the expected output. In other words, the verifications demonstrated code-model equivalence.

The artificial caries lesions were created on the buccal surfaces of human-extracted premolars in this study, and the curvature of the buccal surfaces of these teeth is different than that found on incisors, lower premolars, and molars. Therefore, it was important to ascertain whether the use of the median tangent angle to compute D_{Ia} and D_{Ie} was appropriate and whether it was applicable for other curvatures.

To determine whether the median tangent angle was appropriate, the mean depths of inter- D_{Ie} and intra- prismatic D_{Ia} demineralization zones were computed both with the original surface curvature and with the enamel surface aligned flat. Results showed that the original curvature and the aligned surface were almost identical, indicating that using the median tangent angle was appropriate in the case of upper premolars. During the Phase I verification process, B-scans with different simulated surface curvature (Figure 4) were created from A-scans of pre-determined D_{Ia} and D_{Ie} were created. The D_{Ia} and D_{Ie} output from the algorithm were like the pre-determined ones. This indicates its applicability to other cases of curvature.

The auto-segmentation method of demineralized enamel described here is applicable to demineralized enamel with distinct zones of inter- and intra-prismatic demineralization, therefore making a quantized intensity threshold segmentation of these zones possible. These distinct zones of demineralization are the result of the cyclic nature of demineralization subjected to the samples, the type and pH of the acid used, and the interval of demineralization. Different cyclic protocols, types, and pH of the acid and intervals of demineralization may produce different distributions of inter- and intra- prismatic demineralization. In conditions that produce demineralized enamel with less distinct inter- and intra- prismatic demineralization junctions, such as those in eroded enamel, modification and revalidation of this segmentation technique may be necessary.

The image processing techniques used for the suggested algorithm of this study can be compared with a similar algorithm of a famous research work done by the old, famous, great school of dental image analysis used in OCT for the estimation of lesion severity by Professor Daniel Fried [16, 18, 27, 28, 30, 32, 33, 36, 48]. Regarding the edge-detection approach used in previously developed algorithms, the enamel edge and the lower lesion boundary were determined by applying an edge locator. The program first locates the maximum of each A-scan and differentiates the A-scan maximum as either demineralized or *sound* using the signal-to-noise ratio as a threshold. Another previous method used for edge detection is the anisotropic diffusion filter, which is designed to highlight boundaries, and finally the threshold (Otsu) filter, which is used to identify the position of each edge by identifying the first pixels that fall under the threshold of e^{-2} of the maximum A-scan value. In the suggested algorithm of this study, an intensity threshold of 5 dB was applied to remove the background of the OCT raw frame, and enamel surfaces can be easily detected by scanning the frame for the first non-zero pixel. The location of these pixels is considered the coordinates of the enamel surface. Then the demineralization zone segmentation was applied to the raw OCT frame with the two discrete color zones of demineralization (red: Intra- prismatic, yellow: Inter- prismatic). The last pixel of each zone along each A-scan was considered the axial boundary of each demineralization zone. Therefore, this algorithm can't only distinguish between sound enamel and demineralized enamel but also between each demineralization zone.

In previously developed algorithms, the depth of the lesion was calculated by locating the upper and lower edges using an edge-detection approach. Lesion severity was determined for each A-scan using two different approaches: fixed-depth and edge-detected. In the fixed-depth approach, the enamel surface boundary was determined by the intersection of the line profile A-scan and a manually established straight line that marks the enamel surface in the A-scan. The lesion boundary

was set to an arbitrary depth of 200 μm from the established enamel line. In the suggested algorithm of this study, the demineralization depth was also calculated using two approaches: without and with enamel surface alignment. In the approach without enamel surface alignment, the curvature nature of the enamel surface was considered in the calculation of the demineralization depth of every zone. In enamel surface alignment, the surface of the enamel is aligned to the highest point on the axes of the original enamel surface of the OCT frame and shifts every A-scan up vertically to a new aligned surface level. In both techniques, the average demineralization depth for every demineralization zone has been calculated, and all areas of Intra- prismatic and Inter- prismatic can be calculated.

In conclusion, we have demonstrated that our multi-level quantized intensity threshold segmentation method for demineralized enamel described in this paper can be used to measure inter- and intra-prismatic demineralization zones in artificial enamel caries and verified that there is code-model equivalence. We also demonstrated that the coverage of the model can be extended to various tooth curvatures. We envisage that this algorithm will greatly facilitate the study of the de- and remineralization kinetics of enamel caries lesions and eventually optimize remineralization therapy. Future applications of the algorithm could be used for more enhancements of deep learning segmentation algorithms for OCT scans in demineralization assessment and for the development of real-time oral OCT for clinical diagnostics of early demineralized enamel.

Author Contributions: Conceptualization, T.A. and H.P.C.; methodology, T.A.; software, T.A.; validation, T.A.; formal analysis, T.A. and H.P.C.; investigation, T.A.; resources, H.P.C. and A.F.; data curation, T.A. and M.S.; writing—original draft preparation, T.A.; writing—review and editing, T.A., H.P.C., H.C. and A.F.; visualization, T.A.; supervision, H.P.C and A.F.; project administration, H.P.C.; funding acquisition, H.P.C and A.F.

Funding: This research received no external funding.

Conflicts of Interest: The authors declare no conflict of interest.

References

1. Dai, L.L.; Mei, M.L.; Chu, C.H.; Lo, E.C.M. Remineralizing effect of a new strontium-doped bioactive glass and fluoride on demineralized enamel and dentine. *J Dent* **2021**, *108*, 103633, doi:10.1016/j.jdent.2021.103633.
2. Daneshkazemi, P.; Sadeghian, S.; Khodaei, M. Shear bond strength of orthodontic brackets on intact and demineralized enamel after application of resin infiltrant, fluoride varnish and casein phosphopeptide-amorphous calcium phosphate remineralizing agents: in-vitro study. *Int Orthod* **2021**, *19*, 259-268, doi:10.1016/j.ortho.2021.03.001.
3. Mendes-Gouvea, C.C.; Danelon, M.; Vieira, A.P.M.; do Amaral, J.G.; de Souza Neto, F.N.; Gorup, L.F.; Camargo, E.R.; Delbem, A.C.B.; Barbosa, D.B. Silver nanoparticles associated with a polyphosphate and fluoride enhance the prevention of enamel demineralization and impact on dual-biofilm adhesion. *J Dent* **2022**, *125*, 104245, doi:10.1016/j.jdent.2022.104245.
4. Luiz, M.T.; di Filippo, L.D.; Dutra, J.A.P.; Viegas, J.S.R.; Silvestre, A.L.P.; Anselmi, C.; Duarte, J.L.; Calixto, G.M.F.; Chorilli, M. New Technological Approaches for Dental Caries Treatment: From Liquid Crystalline Systems to Nanocarriers. *Pharmaceutics* **2023**, *15*, doi:10.3390/pharmaceutics15030762.
5. Flemming, J.; Hannig, C.; Hannig, M. Caries Management-The Role of Surface Interactions in De- and Remineralization-Processes. *J Clin Med* **2022**, *11*, doi:10.3390/jcm11237044.
6. El Gezawi, M.; Wolfle, U.C.; Haridy, R.; Fliefel, R.; Kaisarly, D. Remineralization, Regeneration, and Repair of Natural Tooth Structure: Influences on the Future of Restorative Dentistry Practice. *Acs Biomater Sci Eng* **2019**, *5*, 4899-4919, doi:10.1021/acsbiomaterials.9b00591.
7. Nelson, D.G. Backscattered electron imaging of partially-demineralized enamel. *Scanning Microsc* **1990**, *4*, 31-41; discussion 42.
8. Pearce, E.I.; Nelson, D.G. Microstructural features of carious human enamel imaged with back-scattered electrons. *Journal of dental research* **1989**, *68*, 113-118, doi:10.1177/00220345890680020301.
9. Arends, J.; Jongebloed, W.; Ogaard, B.; Rolla, G. SEM and microradiographic investigation of initial enamel caries. *Scandinavian journal of dental research* **1987**, *95*, 193-201, doi:10.1111/j.1600-0722.1987.tb01830.x.
10. Arends, J.; Christoffersen, J. The nature of early caries lesions in enamel. *Journal of dental research* **1986**, *65*, 2-11.
11. Brinkman, J.; ten Bosch, J.J.; Borsboom, P.C. Optical quantitation of natural caries in smooth surfaces of extracted teeth. *Caries research* **1988**, *22*, 257-262.

12. Darling, C.L.; Huynh, G.D.; Fried, D. Light scattering properties of natural and artificially demineralized dental enamel at 1310 nm. *Journal of biomedical optics* **2006**, *11*, 34023, doi:10.1117/1.2204603.
13. Jones, R.; Fried, D. Attenuation of 1310-nm and 1550-nm laser light through sound dental enamel. *Lasers in Dentistry Viii* **2002**, *4610*, 187-190.
14. Schmitt, J.M.; Knuttel, A.; Yadlowsky, M.; Eckhaus, M.A. Optical-coherence tomography of a dense tissue: statistics of attenuation and backscattering. *Phys Med Biol* **1994**, *39*, 1705-1720, doi:10.1088/0031-9155/39/10/013.
15. Colston, B.W., Jr.; Everett, M.J.; Da Silva, L.B.; Otis, L.L.; Stroeve, P.; Nathel, H. Imaging of hard- and soft-tissue structure in the oral cavity by optical coherence tomography. *Appl Opt* **1998**, *37*, 3582-3585.
16. Fried, D.; Xie, J.; Shafi, S.; Featherstone, J.D.; Breunig, T.M.; Le, C. Imaging caries lesions and lesion progression with polarization sensitive optical coherence tomography. *Journal of biomedical optics* **2002**, *7*, 618-627, doi:10.1117/1.1509752.
17. Sowa, M.G.; Popescu, D.P.; Werner, J.; Hewko, M.; Ko, A.C.; Payette, J.; Dong, C.C.; Cleghorn, B.; Choo-Smith, L.P. Precision of Raman depolarization and optical attenuation measurements of sound tooth enamel. *Anal Bioanal Chem* **2007**, *387*, 1613-1619, doi:10.1007/s00216-006-0856-9.
18. Le, M.H.; Darling, C.L.; Fried, D. Methods for calculating the severity of demineralization on tooth surfaces from PS-OCT scans. *P Soc Photo-Opt Ins* **2009**, *7162*, doi:Doi 10.1117/12.816867.
19. Popescu, D.P.; Choo-Smith, L.P.; Flueraru, C.; Mao, Y.; Chang, S.; Disano, J.; Sherif, S.; Sowa, M.G. Optical coherence tomography: fundamental principles, instrumental designs and biomedical applications. *Biophys Rev* **2011**, *3*, 155, doi:10.1007/s12551-011-0054-7.
20. Chew, H.P.; Zakian, C.M.; Pretty, I.A.; Ellwood, R.P. Measuring Initial Enamel Erosion with Quantitative Light-Induced Fluorescence and Optical Coherence Tomography: An in vitro Validation Study. *Caries research* **2014**, *48*, 254-262, doi:10.1159/000354411.
21. Habib, M.; Lee, K.M.; Liew, Y.M.; Zakian, C.; Ung, N.M.; Chew, H.P. Assessing surface characteristics of eroded dentine with optical coherence tomography: a preliminary in vitro validation study. *Appl Opt* **2018**, *57*, 8673-8679, doi:10.1364/AO.57.008673.
22. Besnard, C.; Harper, R.A.; Salvati, E.; Moxham, T.E.J.; Romano Brandt, L.; Landini, G.; Shelton, R.M.; Korsunsky, A.M. Analysis of in vitro demineralised human enamel using multi-scale correlative optical and scanning electron microscopy, and high-resolution synchrotron wide-angle X-ray scattering. *Materials & design* **2021**, *206*, 109739, doi:10.1016/j.matdes.2021.109739.
23. Holtzman, J.S.; Osann, K.; Pharar, J.; Lee, K.; Ahn, Y.C.; Tucker, T.; Sabet, S.; Chen, Z.; Gukasyan, R.; Wilder-Smith, P. Ability of optical coherence tomography to detect caries beneath commonly used dental sealants. *Lasers in surgery and medicine* **2010**, *42*, 752-759, doi:10.1002/lsm.20963.
24. Shimada, Y.; Sadr, A.; Burrow, M.F.; Tagami, J.; Ozawa, N.; Sumi, Y. Validation of swept-source optical coherence tomography (SS-OCT) for the diagnosis of occlusal caries. *J Dent* **2010**, *38*, 655-665, doi:10.1016/j.jdent.2010.05.004.
25. Salehi, H.S.; Granados, A.; Mahdian, M. Comparison of deep convolutional neural network models with OCT images for dental caries classification. *Medical Imaging 2022: Biomedical Applications in Molecular, Structural, and Functional Imaging* **2022**, *12036*, doi:10.1117/12.2613308.
26. Salehi, H.S.; Barchini, M.; Chen, Q.G.; Mahdian, M. Toward development of automated grading system for carious lesions classification using deep learning and OCT imaging. *Medical Imaging 2021: Biomedical Applications in Molecular, Structural, and Functional Imaging* **2021**, *11600*, doi:10.1117/12.2581318.
27. Ei, T.Z.; Shimada, Y.; Abdou, A.; Sadr, A.; Yoshiyama, M.; Sumi, Y.; Tagami, J. Three-dimensional assessment of proximal contact enamel using optical coherence tomography. *Dent Mater* **2019**, *35*, e74-e82, doi:10.1016/j.dental.2019.01.008
28. Chan, K.H.; Chan, A.C.; Fried, W.A.; Simon, J.C.; Darling, C.L.; Fried, D. Use of 2D images of depth and integrated reflectivity to represent the severity of demineralization in cross-polarization optical coherence tomography. *J Biophotonics* **2015**, *8*, 36-45, doi:DOI 10.1002/jbio.201300137.
29. Albelasy, E.H.; Chen, R.; Fok, A.; Montasser, M.; Hamama, H.H.; Mahmoud, S.H.; Abdelrehim, T.; Chew, H.P. Inhibition of Caries around Restoration by Ion-Releasing Restorative Materials: An In Vitro Optical Coherence Tomography and Micro-Computed Tomography Evaluation. *Materials (Basel)* **2023**, *16*, doi:10.3390/ma16165558.
30. Nee, A.; Chan, K.; Kang, H.; Staninec, M.; Darling, C.L.; Fried, D. Longitudinal monitoring of demineralization peripheral to orthodontic brackets using cross polarization optical coherence tomography. *J Dent* **2014**, *42*, 547-555, doi:10.1016/j.jdent.2014.02.011.
31. Shi, B.Y.; Niu, J.X.; Zhou, X.Y.; Dong, X.Y. Quantitative Assessment Methods of Early Enamel Caries with Optical Coherence Tomography: A Review. *Appl Sci-Basel* **2022**, *12*, 8780, doi:ARTN 8780 10.3390/app12178780.
32. Le, M.H.; Darling, C.L.; Fried, D. Automated analysis of lesion depth and integrated reflectivity in PS-OCT scans of tooth demineralization. *Lasers in surgery and medicine* **2010**, *42*, 62-68, doi:10.1002/lsm.20862.

33. Can, A.M.; Darling, C.L.; Ho, C.; Fried, D. Non-destructive assessment of inhibition of demineralization in dental enamel irradiated by a lambda=9.3-microm CO2 laser at ablative irradiation intensities with PS-OCT. *Lasers in surgery and medicine* **2008**, *40*, 342-349, doi:10.1002/lsm.20633.
34. Ravichandran, N.K.; Lakshmikantha, H.T.; Park, H.S.; Jeon, M.; Kim, J. Micron-scale human enamel layer characterization after orthodontic bracket debonding by intensity-based layer segmentation in optical coherence tomography images. *Sci Rep* **2021**, *11*, 10831, doi:10.1038/s41598-021-90354-9.
35. Meng Zhuo, 孟.; X. Steve Yao, 姚.; Yao Hui, 姚.; Liu Tiegen, 刘.; Li Yanni, 李.; Wang Guanhua, 王. Detecting Early Artificial Caries by Using Optical Coherence Tomography. *Chinese Journal of Lasers* **2010**, *37*, 2709-2713, doi:10.3788/cjl20103711.2709.
36. Staninec, M.; Douglas, S.M.; Darling, C.L.; Chan, K.; Kang, H.; Lee, R.C.; Fried, D. Non-destructive clinical assessment of occlusal caries lesions using near-IR imaging methods. *Lasers in surgery and medicine* **2011**, *43*, 951-959, doi:10.1002/lsm.21139.
37. Ravichandran, N.K.; Cho, H.; Lee, J.; Han, S.; Wijesinghe, R.E.; Kim, P.; Song, J.W.; Jeon, M.; Kim, J. An Averaged Intensity Difference Detection Algorithm for Identification of Human Gingival Sulcus in Optical Coherence Tomography Images. *Ieee Access* **2019**, *7*, 73076-73084, doi:10.1109/Access.2019.2920146.
38. Lakshmikantha, H.T.; Ravichandran, N.K.; Jeon, M.; Kim, J.; Park, H.S. 3-Dimensional characterization of cortical bone microdamage following placement of orthodontic microimplants using Optical Coherence Tomography. *Sci Rep* **2019**, *9*, 3242, doi:10.1038/s41598-019-39670-9.
39. Mohamad Saberi, F.N.; Sukumaran, P.; Ung, N.M.; Liew, Y.M. Assessment of demineralized tooth lesions using optical coherence tomography and other state-of-the-art technologies: a review. *Biomed Eng Online* **2022**, *21*, 83, doi:10.1186/s12938-022-01055-x.
40. Rao, Y.; Sarwade, N.P.; Makkar, R. Modeling and Simulation of Optical Coherence Tomography on Virtual OCT. *Procedia Comput Sci* **2015**, *45*, 644-650, doi:10.1016/j.procs.2015.03.121.
41. Abdelrehim, T.; Salah, M.; Sailer, L.; Chew, H.P. Identification of Demineralization Zones in Early Enamel Decay based on Image Correlation between Scanning Electron Microscope (SEM) and Optical Coherence Tomography (OCT).
42. *Optical Coherence Imaging Techniques and Imaging in Scattering Media Iv* **2021**, *11924*, doi:Artn 119241e10.1117/12.2616136. White, D.J.; Featherstone, J.D. A longitudinal microhardness analysis of fluoride dentifrice effects on lesion progression in vitro. *Caries research* **1987**, *21*, 502-512.
43. Mathworks. Image processing toolbox help, MATLAB®. Available online: http://www.mathworks.com/ (accessed on 22 October 2023).
44. Guan, A.; Richardson, S.; Hinckley, S. Optical coherence tomography modeling incorporating scattering, absorption, and multiple reflections. *J Opt Soc Am A Opt Image Sci Vis* **2020**, *37*, 391-398, doi:10.1364/JOSAA.377121.
45. J M Schmitt , A.K., M Yadlowsky and M A Eckhaus. Optical-coherence tomography of a dense tissue: statistics of attenuation and backscattering. *Physics in Medicine & Biology* **1994**, *39*, 1705, doi:10.1088/0031-9155/39/10/013.
46. Meiburger, K.M.; Salvi, M.; Rotunno, G.; Drexler, W.; Liu, M.Y. Automatic Segmentation and Classification Methods Using Optical Coherence Tomography Angiography (OCTA): A Review and Handbook. *Appl Sci-Basel* **2021**, *11*, doi:10.3390/app11209734.
47. De Jesus, D.A.; Brea, L.S.; Breda, J.B.; Fokkinga, E.; Ederveen, V.; Borren, N.; Bekkers, A.; Pircher, M.; Stalmans, I.; Klein, S.; et al. OCTA Multilayer and Multisector Peripapillary Microvascular Modeling for Diagnosing and Staging of Glaucoma. *Transl Vis Sci Techn* **2020**, *9*, doi:10.1167/tvst.9.2.58.
48. Kang, H.; Jiao, J.J.; Lee, C.; Le, M.H.; Darling, C.L.; Fried, D. Nondestructive Assessment of Early Tooth Demineralization Using Cross-Polarization Optical Coherence Tomography. *IEEE Journal of Selected Topics in Quantum Electronics* **2010**, *16*, 870-876, doi:10.1109/jstqe.2009.2033610.
49. Rokach, L.; Maimon, O. Clustering Methods. In *Data Mining and Knowledge Discovery Handbook*; Springer: Boston, MA, USA, 2005; pp. 321 - 352.
50. Taibouni, K.; Chenoune, Y.; Miere, A.; Colantuono, D.; Souied, E.; Petit, E. Automated quantification of choroidal neovascularization on Optical Coherence Tomography Angiography images. *Computers in Biology and Medicine* **2019**, *114*, doi:10.1016/j.compbiomed.2019.103450.
51. Engberg, A.M.E.; Erichsen, J.H.; Sander, B.; Kessel, L.; Dahl, A.B.; Dahl, V.A. Automated Quantification of Retinal Microvasculature from OCT Angiography Using Dictionary-Based Vessel Segmentation. *Comm Com Inf Sc* **2020**, *1065*, 257-269, doi:10.1007/978-3-030-39343-4_22.
52. Kaur, D.; Kaur, Y. Various image segmentation techniques: a review. *International Journal of Computer Science and Mobile Computing* **2014**, *3*, 809-814.